

## Li-Ion Batteries

How to cite: *Angew. Chem. Int. Ed.* **2020**, 59, 14313–14320

International Edition: doi.org/10.1002/anie.202005337

German Edition: doi.org/10.1002/ange.202005337

# Size-Mediated Recurring Spinel Sub-nanodomains in Li- and Mn-Rich Layered Cathode Materials

Biwei Xiao<sup>+</sup>, Hanshuo Liu<sup>+</sup>, Ning Chen<sup>+</sup>, Mohammad Norouzi Banis, Haijun Yu, Jianwen Liang, Qian Sun, Tsun-Kong Sham, Ruying Li, Mei Cai,\* Gianluigi A. Botton,\* and Xueliang Sun\*

**Abstract:** Li- and Mn-rich layered oxides are among the most promising cathode materials for Li-ion batteries with high theoretical energy density. Its practical application is, however, hampered by the capacity and voltage fade after long cycling. Herein, a finite difference method for near-edge structure (FDMNES) code was combined with in situ X-ray absorption spectroscopy (XAS) and transmission electron microscopy/electron energy loss spectroscopy (TEM/EELS) to investigate the evolution of transition metals (TMs) in fresh and heavily cycled electrodes. Theoretical modeling reveals a recurring partially reversible  $\text{LiMn}_2\text{O}_4$ -like sub-nanodomain formation/dissolution process during each charge/discharge, which accumulates gradually and accounts for the Mn phase transition. From the modeling of spectra and maps of the valence state over large regions of the cathodes, it was found that the phase change is size-dependent. After prolonged cycling, the TMs displayed different levels of inactivity.

Li- and Mn-rich transition metal (TM) oxides, with a general chemical formula of  $x\text{Li}_2\text{MnO}_3 \cdot (1-x)\text{LiMeO}_2$  (Me = Mn, Ni, Co etc.) (LMR-NMC) have been regarded as some of the most promising cathode materials for the next generation of high-energy-density lithium-ion batteries (LIBs).<sup>[1]</sup> Different from conventional layered  $\text{LiMeO}_2$ , excess lithium ions reside in the TM layers, forming an intergrown  $\text{Li}_2\text{MnO}_3$  crystal domain with  $\text{LiMn}_6$  units in the parent  $\text{LiMeO}_2$  structure.<sup>[2]</sup> The combination of the  $C2/m$   $\text{Li}_2\text{MnO}_3$  and the  $R\bar{3}m$   $\text{LiMeO}_2$  crystal domains has allowed this material to deliver a capacity of over  $250 \text{ mAh g}^{-1}$  within a voltage window of 2.0–4.6 V (vs.  $\text{Li/Li}^+$ ), which represents the highest energy density reported so far in LIB cathode materials.<sup>[3]</sup>

Currently, it is believed that the high capacity in LMR-NMC is achieved by sacrificing its structure integrity. This is a result of Mn migration into the Li layer after oxygen release, forming a spinel structure.<sup>[4]</sup> It severely blocks the Li-ion diffusion pathways, ending up with a very poor rate capability.<sup>[5]</sup> On the other hand, the agglomeration of the spinel phase leads to the decay of average voltage and results in the loss of energy density of the whole cell.<sup>[6]</sup> The migration of the TMs has also been studied by many researchers through microscopic characterization; each of the TMs tends to undergo different migration pathways and segregate from each other.<sup>[6b,7]</sup> Despite the well-accepted phase transition mechanism, there still remain many unresolved questions in the LMR-NMC. First, even though the layer to spinel phase transition has been identified, more efforts are needed to investigate the incubation and reversibility of this process.<sup>[8]</sup> Second, how the TMs participate in the charge compensation of the charge/discharge process after the long-term cycling process is not clear. The fact that each of the TMs favors certain migration pathways could eventually lead to divergent electrochemical behaviors, hence it is of major significance to identify the evolution of each TM individually.<sup>[9]</sup> In order to deal with these questions, it is essential to utilize an approach that can probe the local information of the TMs in an in situ manner. In situ XRD, HRTEM, NMR, and so forth have been reported, but they have certain limitations.<sup>[10]</sup> In situ XRD only probes phases that are large enough with ordered structure, hence the incubation period of the phase development cannot be evaluated. HRTEM relays local information down to atomic scale, but it is not element specific. An in situ operation has been very challenging and an electron beam

[\*] Dr. B. Xiao,<sup>[†]</sup> Dr. M. N. Banis, Dr. J. Liang, Dr. Q. Sun, R. Li, Prof. X. Sun  
 Department of Mechanical and Materials Engineering  
 University of Western Ontario  
 London, Ontario, N6A 6B9 (Canada)  
 E-mail: xsun@eng.uwo.ca

Dr. H. Liu,<sup>[†]</sup> Prof. G. A. Botton  
 Department of Materials Science and Engineering  
 McMaster University  
 Hamilton, ON L8S 4L8 (Canada)  
 E-mail: gbotton@mcmaster.ca

Dr. N. Chen,<sup>[†]</sup> Prof. G. A. Botton  
 Canadian Light Source  
 Saskatoon, SK, S7N 2V3 (Canada)



Prof. H. Yu  
 College of Materials Sciences and Engineering  
 Key Laboratory of Advanced Functional Materials

Education Ministry of China, Beijing University of Technology  
 Beijing 100124 (P. R. China)

Prof. T.-K. Sham  
 Department of Chemistry, University of Western Ontario  
 London, Ontario, N6A 5B7 (Canada)

Dr. M. Cai  
 General Motors Research & Development Center  
 Warren, MI 48090-9055 (USA)  
 E-mail: mei.cai@gm.com

[†] These authors contributed equally to this work.

 Supporting information and the ORCID identification number(s) for the author(s) of this article can be found under:  
 <https://doi.org/10.1002/anie.202005337>.

hitting the sample, especially under operating conditions, may cause undesired impact that makes the result unreliable.<sup>[11]</sup> Most NMR experiments probe the local environment of Li but cannot give information about the environment of Mn/Co/Ni, not to mention that the material tends to lose Li upon cycling.<sup>[12]</sup>

X-ray absorption near-edge spectroscopy (XANES), which enables the detection of core-electron excitation processes of TMs, has been widely used to probe the local structure of LIB materials in the sub-nanometer range. TM K- and L-edge XANES, with its dipole selection rules, can provide abundant information on the electronic configuration and oxidation state of TMs, therefore they have been extensively used for understanding the structural changes of cathode materials.<sup>[13]</sup> In situ XANES of the first and subsequent cycles of LMR-NMC have been conducted, the charge compensation mechanism has been investigated in these reports using the XANES region, and the surrounding environment was evaluated based on the EXAFS results.<sup>[14]</sup> By collecting EXAFS, what one gets is only averaged first TM–O coordination and second TM–TM coordination in multiple species, hence phase speciation is not possible. Regarding this, it is of great interest to better utilize the XANES part and explore from different perspectives.<sup>[14a,15]</sup> There are two parallel approaches for XANES speciation. The first approach is solely based on the experimental data from model compound standards. This approach works well under the condition that model compounds in the standard system are correctly selected, not only from speciation and crystallography perspectives, but also with regards to the local structural environment for the corresponding element of interest. Unfortunately, these prerequisites are not available for some XANES cases, including the research reported herein. The XANES approach based on theoretical modeling is especially powerful when dealing with a system experiencing a dynamic course, for example, the redox-related partially reversible crystallization and dissolution process that occurs during multiple charging and discharging of batteries. Then the only option is to take a second approach, which relies at least partially on XANES theoretical calculation to provide certain standard spectra for corresponding speciation, followed by linear combination fitting (LCF) analysis. Either the finite difference method for near-edge structure (FDMNES) or FEFF has been used in this regard.<sup>[16]</sup> In this study, a FDMNES code was combined with in situ XANES measurement and transmission electron microscopy and electron energy loss spectroscopy (TEM/EELS) mapping to track the evolution of TMs in both the first and 451<sup>st</sup> cycles. The development of the surrounding environment of Mn has been well reproduced with a partially reversible formation/dissolution of a LiMn<sub>2</sub>O<sub>4</sub>-like sub-nanodomain during the charging/discharging process. It accounts for the accumulation of the spinel phase after long-term cycling. The phase accumulates predominantly in small particles and on the surface of large particles. This study offers new insights for the development of LMR-NMC cathode materials.

The chemical composition of the LMR-NMC was measured by inductively coupled plasma atomic emission spectrometry (ICP-OES). The relative Mn:Co:Ni ratio was

found to be 67:16:17, which is close to the theoretical stoichiometry of 68:16:16 according to the chemical formula of Li<sub>1.2</sub>Mn<sub>0.54</sub>Co<sub>0.13</sub>Ni<sub>0.13</sub>O<sub>2</sub>. SEM images of the fresh electrode and the electrode after 450 cycles are presented in Figure S1, the original LMR-NMC particles are around 100 nm in size (Figure S1a). The LMR-NMC material was cycled at C/2 rate (1 C = 250 mAh g<sup>-1</sup>) after an initial activation cycle at C/20. After cycling, although the size of the particles remains almost unchanged, the particles are covered by a dense film (Figure S1b). Chemical analysis of the O 1s XPS (Figure S1c,d) has revealed that the cycled sample contains a large amount of C=O and C–O groups that belong to the solid electrolyte interphase (SEI).<sup>[13d]</sup> The initial charge capacity was 303 mAh g<sup>-1</sup> and the initial discharge capacity was 253 mAh g<sup>-1</sup>, as shown in Figure 1a. The large irreversible capacity in this material due to the loss of active Li<sup>+</sup> is detrimental for practical full-cell configurations with a limited Li amount. The capacity shows dramatic decay after long-term cycling; only 123 mAh g<sup>-1</sup> discharge capacity was obtained in the 450<sup>th</sup> cycle. Figure 1b shows the charge/discharge curves of the 1<sup>st</sup>, 2<sup>nd</sup>, 50<sup>th</sup>, 100<sup>th</sup>, 200<sup>th</sup>, and 450<sup>th</sup> cycles. In the initial charge process, the slope below 4.45 V has been ascribed to the de-intercalation of Li ions from the R $\bar{3}m$  LiMeO<sub>2</sub> phase.<sup>[1]</sup> Followed by this, a long plateau due to the release of oxygen from the edges of the LiO<sub>6</sub> octahedra in the C2/m Li<sub>2</sub>MnO<sub>3</sub> emerged. The oxygen release promotes the electrolyte decomposition and structural deterioration.<sup>[17]</sup> The capacity drop during cycling was accompanied by a voltage drop as shown in the charge/discharge curves of the following cycles. The dQ/dV curves of the 1<sup>st</sup> and 450<sup>th</sup> cycles are illustrated in Figure 1c. All the capacity was delivered above 3.0 V in the first cycle, yet after 450 cycles, the capacity above 3.0 V became marginal. Such a voltage drop has been regarded as the biggest hindrance in the commercialization of LMR-NMC materials.<sup>[1]</sup> Notable studies have been carried out to understand this behavior, the majority of which

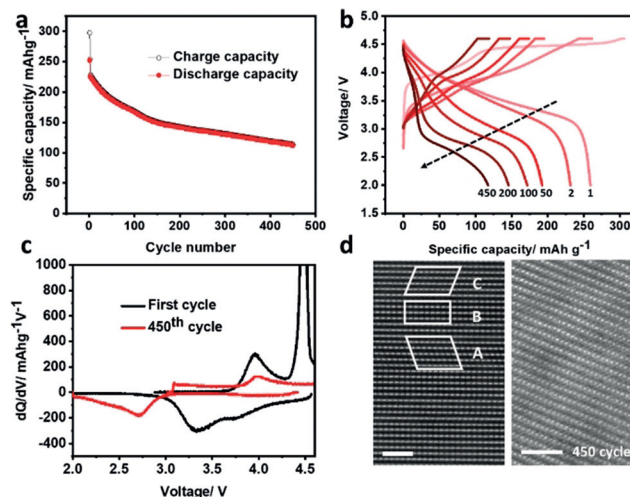


**Figure 1.** a) Cycling performance of the LMR-NMC. b) Charge/discharge curves of the 1<sup>st</sup>, 2<sup>nd</sup>, 50<sup>th</sup>, 100<sup>th</sup>, 200<sup>th</sup>, and 450<sup>th</sup> cycle. c) dQ/dV curves of the initial cycle and the 450<sup>th</sup> cycle. d) Aberration-corrected STEM image of the pristine LMR-NMC and LMR-NMC cycled 450 times. Scale bar: 2 nm.

believed that the voltage drop was closely associated with the irreversible phase transformation from layered to spinel and/or rock salt phases.<sup>[6d,11,18]</sup>

Atomic resolution STEM images of the fresh LMR-NMC particle have been collected and shown in Figure 1 d. The Li-TM-TM dumbbell structure can be clearly seen in the TM layers of the pristine LMR-NMC due to the excess Li in the TM layers (Figure 1 d, left panel). Note that the contrast of the HAADF-STEM image is proportional to the Z-number of the elements present in the material. In this case, the bright atomic columns are the heavier TM atoms, and the lighter elements, Li and O, are not visible in the image. Regions A, B, and C represent different stacking sequences of the TMs and Li atoms, which correspond to the projection of [110], [100], and [110] orientations of the  $C2/m$  monoclinic structure; such stacking faults have also been observed from previous studies.<sup>[2,18c]</sup> These monoclinic dumbbell features are no longer visible in the LMR-NMC cycled 450 times (Figure 1 d, right panel). The remaining layered phase has mostly transformed into a conventional NMC-type ( $R\bar{3}m$ ) phase accompanied with the loss of TM layer Li. The change is also evident in the X-ray diffraction (XRD) patterns (Figure S2a,b). In the pristine LMR-NMC sample, the presence of the diffraction peaks at around  $20^\circ$  indicates the presence of superlattice ordering arising from the excess Li atoms in the TM layers,<sup>[19]</sup> which disappeared in the sample cycled 450 times; the sharp peak at close position is ascribed to the diffraction from  $\text{Li}_2\text{CO}_3$ .<sup>[20]</sup> In the meantime, spinel and rock salt phases were identified in the XRD and RAMAN spectra (Figure S2b,c).

The in situ XANES measurements of the Mn K-edges of the first and 451<sup>st</sup> cycles are shown in Figure 2 a–d. Figure 2 a displays the Mn K-edge XANES of the charging process. Overall, four trends are observed. Trend  $\alpha$  represents a development of the white line, which is in fact a multiple scattering since it appears significantly above the threshold; its intensity decreases and its position is drifting in the higher energy direction, indicating a shortening of the Mn–O distance on average since in multiple scattering theory, the position of the resonance above the threshold is inversely proportional to the square of the interatomic distance. Thus, the farther away the resonance from the threshold, the shorter the bond. Meanwhile the trend  $\beta$  indicates the progressive change of the edge jump line-shape from concave to convex (change of the densities of states of Mn p character in the conduction band). Trends A and B shown in the inset are the progressive increase of pre-edge feature of the Mn K-edge XANES, assigned to the dipole-forbidden transition of 1s to 3d states; they usually appear to be very weak in highly ordered octahedral coordination. However, due to the mixing of the 4p and 3d states, an electric quadrupole-allowed transition has contributed to the pre-edge peak; therefore, the pre-edge peaks are enhanced. Peak A at lower energy of the doublet can be assigned to the transition from 1s to  $t_{2g}$  energy level and Peak B at higher energy can be assigned to the transition from 1s to  $e_g$  energy level.<sup>[14a]</sup> Trends A and B have been attributed to the distortion of the  $\text{MnO}_6$  octahedra in most of the in situ XANES work; higher intensities of these two peaks imply more distorted structure.<sup>[14a,21]</sup> During discharge, as shown in Figure 2 b, the four XANES features show reverse changing

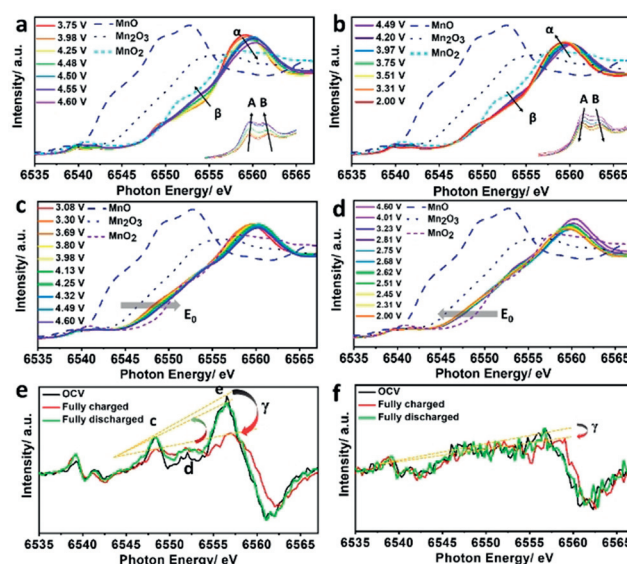


**Figure 2.** In situ Mn K-edge XANES system recorded throughout a) initial charging process (inset: pre-edge regions), b) initial discharging process (inset: pre-edge regions), c) the 451<sup>st</sup> charging process, d) 451<sup>st</sup> discharging process. e, f) First-derivative peaks of the Mn K-edge XANES edge jump data range for LMR-NMC at OCV, fully charged and fully discharged states during e) the first cycle, and f) the 451<sup>st</sup> cycle.

trends, with Trend  $\alpha$  shifting upward, Trend  $\beta$  shifting downward, and Trends A and B moving to lower intensity, revealing opposite Mn local structural adjustment trend between the charging and discharging reactions.

During the 451<sup>st</sup> cycle, the evolution of Mn K-edge XANES spectra becomes subtle, especially for the extent of change between the starting and ending of the discharge process for trends A and B (Figures 2c,d), and  $\beta$  for the discharging process (Figure 2d), suggesting that the given reaction has almost stopped. These experimentally resolved XANES data trends evolved stepwise with the performance of the cell, suggesting that the Mn K-edge XANES and the data trends are fingerprint features for the performance degradation of the cell throughout the charging and discharging process.

While tracing the local environment of Mn using XAS has been carried out in many previous in situ XAS studies, it remains elusive as to how to correlate the Mn local structural environment and Mn speciation with the evolution of the cell performance. In this study, we attempt to address the Mn local environment by examining the line-shape of the edge jump using the first-derivative spectra of the Mn K-edge XANES shown in Figure 2 e,f. In the pristine LMR-NMC material, three characteristic peaks appear in the energy range of 6545–6560 eV at the beginning of the first cycle of charging with the intensity of the peak labeled e being much more intense than the other two. However, upon charging, the intensity of peak e decreases significantly, eventually showing a flat triplet feature with roughly equal intensities at the end of the charging process. The trend is marked as  $\gamma$  in the figures, which is the angle between starting and ending point of a charging and discharging process (the yellow lines are

defined as the connection of peaks c and e) (Figure 2 e). When the material was fully charged and tuned to the reverse discharging process, the reverse  $\gamma$  trend takes place, but is unable to return to the original angle position of the fresh LMR-NMC material (Figure 2 e). Such an incomplete conversion implies that there was a partially reversible transition in the material. A complete set of the first-derivative plots is shown in Figure S3; the  $\gamma$  trend is obvious in the beginning and becomes gradually weaker at the end of charging/discharging. Further examination of the first-derivative peaks of the Mn K-edge XANES of the 451<sup>st</sup> cycle (Figure 2 f) shows that the angle changing of the  $\gamma$  trend becomes almost negligible compared to the first cycle; the first-derivative spectra feature the triplet peak with almost equivalent intensity throughout the whole process. The sharp contrast between the initial cycle and the 451<sup>st</sup> cycle, along with the partially reversible  $\gamma$  trend in the first cycle imply that a second less active Mn domain/phase that features the triplet peaks with close intensities emerges when charging is started. During the discharging process, the above process was reversed, but not completely. After extensive cycles, the accumulation of the related Mn domain becomes significant, and it is likely to be associated with the cell performance decay.

To address the structural and chemical significance of the experimentally revealed XANES features A, B,  $\alpha$ , and  $\beta$ , and the flat triplet feature  $\gamma$  characterized at the XANES edge jump of Mn K-edge XANES (Figure 2), XANES theoretical modeling was performed by using the FDMNES code.<sup>[22]</sup> A corresponding structure system was first developed, which is composed of Mn-centered and spherical particles or domains with progressively increasing domain radii. FDMNES modeling was first performed on each particle of the system to develop the corresponding theoretical XANES system. Then the best fit XANES was identified based on the comparison between experimental data vs. modeled XANES spectra.

At first, the Mn K-edge XANES of  $\text{LiNi}_{1/3}\text{Mn}_{1/3}\text{Co}_{1/3}\text{O}_2$  was modeled using a hexagonal  $\text{Li}_3\text{MnCoNiO}_6$  structure as shown in Figure S4 (details of the modeling process can be found in the experimental section). By adjusting the size of the Mn-centered domain, a series of Mn K-edge XANES of  $\text{Li}_3\text{MnCoNiO}_6$  have been obtained. In order to validate the modeling result, the calculated XANES spectra have been paired with the experimentally collected  $\text{Li}_2\text{MnO}_3$  Mn K-edge XANES results using linear combination fitting (LCF). The LCF best fit has been achieved using a calculated XANES based on a domain radius of  $5.5 \text{ \AA}$  (R5.5) as one of the standard spectra of  $\text{LiNi}_{1/3}\text{Mn}_{1/3}\text{Co}_{1/3}\text{O}_2$  and experimental XANES model compound from  $\text{Li}_2\text{MnO}_3$  as the second standard spectrum as shown in Figure S5. This approach gives an estimation that the LMR-NMC constitutes 75%  $\text{Li}_2\text{MnO}_3$  and 25%  $\text{Li}_3\text{MnCoNiO}_6$ . The nominal composition of this LMR-NMC is  $\text{Li}[\text{Li}_{0.2}\text{Mn}_{0.54}\text{Co}_{0.13}\text{Ni}_{0.13}]\text{O}_2$ , which can also be written as the combination of  $0.41 \text{ Li}_2\text{MnO}_3 + 0.13 \text{ Li}_3\text{MnCoNiO}_6$ , with the actual percentage of the  $\text{Li}_2\text{MnO}_3$  phase being approximately three times that of  $\text{Li}_3\text{MnCoNiO}_6$ . The agreement between the XANES LCF analysis and the actual chemical composition indicates that the theoretical modeling of the XANES spectra using

FDMNES code is a valid approach to evaluate the experimental data under favorable conditions.

A complete set of possible Mn-bearing phases were modeled; the results are shown in Table 1 in the Supporting Information. Within these simulated Mn phases,  $\text{LiMn}_2\text{O}_4$ -like spinel phase uniquely displays a triplet feature in the first derivative of the Mn K XANES edge jump with equivalent peak intensities throughout the triplet feature, which is shown in Figure 3 a. With the increase of the Mn-centered domain size, the triplet peak feature starts to emerge at a radius of  $5.0 \text{ \AA}$  and is maintained beyond this limit, suggesting that overall a scale of nanometer in diameter is the critical size for the  $\text{LiMn}_2\text{O}_4$ -like domain to resolve the feature. The triplet peak feature of  $\text{LiMn}_2\text{O}_4$  has also been observed in the experimentally obtained Mn K-edge XANES from model compound  $\text{LiMn}_2\text{O}_4$  shown in Figure S6, suggesting that the simulation is valid.

To analyze the aging process of the LMR-NMC material, the modeled Mn K-edge XANES of  $\text{LiMn}_2\text{O}_4$  phase with increasing domain radius is shown in Figure 3 b–d. The experimentally resolved four feature trends, that is,  $\alpha$ ,  $\beta$ , A, and B, have all been very well resolved and reproduced throughout the simulated  $\text{LiMn}_2\text{O}_4$  XANES system. Note that Trends A and B appear to be increasing in step as shown in Figure 3 c,d. Peaks A and B are contributed by the backscattering from the Mn local structural environment of different coordination shells. As shown in Figure 3 c, at R2.0 only the backscattering from the first shell octahedral

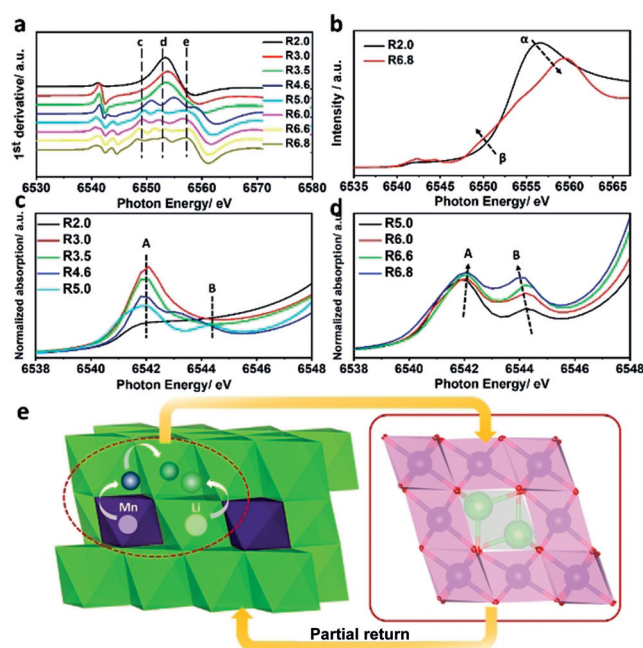


**Figure 3.** a) First derivatives of the simulated  $\text{LiMn}_2\text{O}_4$  Mn K-edge XANES system with various domain sizes. b) Simulated  $\text{LiMn}_2\text{O}_4$  Mn K-edge XANES showing trends  $\alpha$  and  $\beta$ . c,d) Pre-edge features of the simulated Mn K-edge XANES of  $\text{LiMn}_2\text{O}_4$  with various domain sizes, revealing the impact from particle size to features A and B, respectively, with radius of  $\approx 5.0 \text{ \AA}$  as critical size for the effect. e) Schematic diagram showing potential formation route of the spinel-like  $\text{LiMn}_2\text{O}_4$  in the  $\text{Li}_2\text{MnO}_3$  component (blue sphere: Mn, green sphere: Li).

coordination of Mn–O bonding is experienced by the center absorbing Mn, resulting the precursor of feature peak A. When the backscattering of the second shell Mn–Mn coordination (covered by cluster R3.0) joins the pre-edge feature effect, strong positive interference occurred between the signal from the Mn–Mn scattering related peak and that of the first shell Mn–O scattering with the intensity of A strangely enhanced. With the additional backscattering from atoms up to R3.5, the precursor of the feature B begins to grow at the low-energy side of the final position of feature B. Induced by negative peak interference from these further scattering, the intensity of A is reduced. When the backscattering is extended to R4.6, precursor B is further enhanced in-step with decrease in A from further negative peak interference; this effect further occurred to A up to cluster R5.0. At this cluster size, the feature clearly results at  $\approx 6544.5$  eV. Since XAFS is a single-electron process and XANES spectrum is analyzed in a normalized scenario, the overall transition probability for features A and B is roughly constant throughout the progressively developing process. Therefore, the evolution of A and B and their relative change is linked to the development of the spinel-type precursor up to the nano scale (i.e., R5.0). As shown in Figure 3d, after R5.0, the further growth of the spinel-type structure is demonstrated by the progressive development of the B rather than A peak. The slight increase in A is induced at first by the progressive increase of B as background signal, and further induced by the progressive increase in the edge-jump signal as the second part of the background signal. The major significance of the modeling from R5.0 to R6.8 is to address the dynamic development of the domain size of the spinel structure from R5.0 to R6.8. Therefore, the herein reported systematic modeling results reveal that the progressive evolution of A and B and their relative change is the fingerprint feature to address the dynamic development process of the spinel type structure in the sample system. The modeling also indicates that the R5.0 cluster is a critical size. When the spinel structure is developed up to R5.0, B is well-resolved at  $\approx 6544.5$  eV. With B further developed vs. A, the size of the spinel structure is further developed beyond the nano scale. This inconsistency in feature trends further correlates the experimental result (Figure 3a) to the domain size of  $\text{LiMn}_2\text{O}_4$ , revealing that the distribution of domain sizes in the actual material may vary largely, and the particle size effect directly impacts the XANES feature. Trend A is mainly regulated by the change of  $\text{LiMn}_2\text{O}_4$ -type of small domains up to 5 Å in radius, while Trend B is due to the change of larger domains with radius  $\geq 5$  Å.

The well-resolved simulation results suggest that the  $\text{LiMn}_2\text{O}_4$ -like domain is an ideal mathematic solution and poses the speculation that the experimentally obtained in situ Mn K-edge XANES is indicative of the development of  $\text{LiMn}_2\text{O}_4$  domains within the particle. The system under investigation has multiple coexisting Mn phases ( $\text{Li}_2\text{MnO}_3$  and LiNMC), resulting in peak interference effects among backscattering from different scattering paths of the same Mn phases and a similar type of backscattering from different species. This effect makes data interpretation for the post white-line XANES features and EXAFS feature very diffi-

cult. In the  $\text{LiMn}_2\text{O}_4$  spinel species the Mn oxidation state is slightly lower than in other coexisting Mn phases in the system. This unique XANES feature is critical, which makes the experimentally resolved pre-edge features A and B, the triple features with equivalent intensities of the first-derivative XANES, and their corresponding data trends unique fingerprint features in this study in terms of Mn speciation and understanding of the dynamic process of battery performance. During charging, the sub-nanometer domain with  $\text{LiMn}_2\text{O}_4$ -type structure grows gradually. During discharging, the domain size decreases gradually yet cannot fully disappear at the end of discharge. Similar XANES features A, B,  $\alpha$ , and  $\beta$  are also observed in some other in situ XAS studies of regular layered  $\text{LiNi}_x\text{Mn}_y\text{Co}_{1-x-y}\text{O}_2$ ,<sup>[21a,23]</sup> since the spinel  $\text{LiMn}_2\text{O}_4$ -type structure is involved in these materials as well.

As shown in Figure 3e, to form a spinel  $\text{LiMn}_2\text{O}_4$ -like phase, Mn needs to migrate to the octahedral site in the Li layer following a  $\text{TM}_{\text{oct}}\text{-Li}_{\text{tet}}\text{-Li}_{\text{oct}}$  pathway.<sup>[24]</sup> In the meantime, Li from the Li layer reversibly migrates to the adjacent tetrahedral site.<sup>[24,25]</sup> Both reversible and irreversible migrations of Mn in LMR-NMC have been reported.<sup>[26]</sup> The reversible migration is the process where the tetrahedral site in the Li layer is occupied at a metastable state and it is responsible for the voltage hysteresis; this is, however, not a spinel phase. The irreversible migration is arguably the process where the Mn migrates through the metastable site to a cubic environment (i.e. the next octahedral site); this is when spinel phase forms. Previous ex situ TEM studies have argued that there might be a partially reversible spinel phase formation during the charging/discharging process,<sup>[8a]</sup> which supports the XANES experimental observation and the corresponding XANES theoretical modeling of this work. At the end of each cycle, some  $\text{LiMn}_2\text{O}_4$ -like sub-nanodomains survive, which accumulate and become actual phases after long-term cycling; this has been verified by the XRD and RAMAN spectra of the sample after 450 cycles as shown in Figure S2a–c. Additionally, the Fourier transform spectra of Mn K-edge EXAFS data of the fresh electrode, the electrode after one cycle, and the electrode cycled 450 times are shown in Figure S2d. The intensity of the first Mn–O shell drops obviously after 450 cycles; it could be associated with both oxygen vacancies and lower coordination number (i.e. tetrahedral instead of octahedral coordination; it is evidence of the presence of the spinel phase).

The transformation to a spinel-like phase for Mn is accompanied by a reduction of its oxidation state. To further study the change of TM after prolonged cycles, the TM  $L_{3,2}$ -edge XANES were collected using soft X-ray under both total electron yield (TEY) and fluorescence yield (FLY), as shown in Figures S7 and S8. The TEY mode collects information up to a depth of 5 nm on the surface of the specimen and the FLY mode can penetrate to a depth of more than 100 nm into the bulk.<sup>[27]</sup> After 450 cycles, both Mn and Co were heavily reduced on the surface and moderately reduced in the bulk, whereas Ni remains divalent (Figure S7a–c). The reason why reduction is not observed only in Ni is because  $\text{Ni}^{2+}$  cannot be further reduced. The reduction of TMs is also shown in the O K-edge XANES collected in FLY mode as shown in Figure S7d. The pre-edge corresponds to the excitation of O 1s

electron to the hybridization of O 2p and TM 3d orbitals. The intensity drop indicates fewer electron vacancies to be filled by the core electron, which reveals reduced TMs and corroborates the TM L-edge XANES results.

The reason for the heavy reduction of Mn and Co can be ascribed to several possibilities. First, at fully charged state, these TMs are highly oxidizing; they tend to react with the electrolyte and end up being reduced and form species such as metal fluorides.<sup>[5b]</sup> Second, oxygen and Li loss from the structure can induce the TM reduction.<sup>[28]</sup> Once the  $\text{Mn}^{4+}$  are reduced to  $\text{Mn}^{3+}$ , the Jahn–Teller effect of the  $\text{Mn}^{3+}$  results in the formation of  $\text{Mn}^{2+}$ .  $\text{Mn}^{2+}$  ions are known to be prone to diffusion into the tetrahedral sites between two octahedral sites and form a spinel phase. The  $\text{LiMn}_2\text{O}_4$ -like spinel structure simulated by FDMNES in the first cycle could gradually turn into a  $\text{Mn}_3\text{O}_4$ -like spinel structure accompanied by the loss of Li.<sup>[5b,29]</sup>

To visualize the reduction of the TMs at a high spatial resolution, electron energy loss spectroscopy (EELS) data of the LMR-NMC cycled 450 times was collected and used to generate the Mn valence map using the multiple linear least square method since there is a very clear shift in the Mn M and L edges from the surface of the particles compared to the bulk regions. As shown in Figure 4 a,b, although Mn remains in the tetravalent state in the bulk region of the large LMR-NMC particles, there is a significant portion of active material being reduced to lower oxidation state. Most of the near surface areas of the large particles and the entire small particles have been reduced. The significantly heavier reduction in small particles can be associated with more contact

area with the electrolyte and shorter length for oxygen vacancy diffusion to the surface that exacerbates the oxygen release.<sup>[30]</sup> Such a heterogeneous valence reduction signifies the importance of material size homogeneity and structural perfection. However, it is believed that in order to achieve high rate capability, the particle size is desired to be small for shorter Li-ion diffusion routes.<sup>[31]</sup>

The observation of higher reduction in small particles implies that it is essential to balance the size distribution to achieve both short diffusion and low reduction simultaneously. Figure S9 shows a comparison of LMR-NMC performances with different particle sizes. Figure S9a,b shows that the size of the small size (SS) LMR-NMC falls in the range of 100–200 nm and that of the large size (LS) LMR-NMC falls in the range of 1–2  $\mu\text{m}$ . XRD patterns of these two samples (Figure S9c) show no difference in their phases. As shown in Figure S9d, the performance of SS-LMR-NMC is better than that of LS-LMR-NMC in the beginning; this is because of shorter diffusion distance and hence higher capacity. After cycling for more than 60 cycles, the SS-LMR-NMC sample becomes unstable and the stability drops obviously. Comparing the corresponding  $dQ/dV$  curves of these two samples after 100 cycles (Figure S9e), SS-LMR-NMC demonstrates more phase transition to spinel structure (the discharge peak at  $< 3.0$  V is the evidence of such transition), which agrees with our observation that small particles suffer from more surface change. Within the first tens of cycles, the performance of LMR-NMC is mediated by the diffusion length, whereas after a certain number of cycles, the performance starts to be dictated by the irreversible reduction.

The atomic-resolution STEM image acquired from a reduced small particle exhibits the MO-type rock-salt structure (Figure 4c); the corresponding Fourier transform diffractogram and atomic model are shown in Figure S10a,b. Surface reconstruction layers have also been discovered on the surface of large particles (Figure S10c,d). The results confirm that the reduced areas underwent structural transformation.<sup>[32]</sup> In accordance, the core-loss EELS spectrum (Figure 4d,e) acquired from the Mn-reduced region suggests that Co has also been reduced to a lower oxidation state, as evidenced by the shift of the Co L-edge towards lower energy. In addition, as can be seen from Figure 4d, the Li K-edge from the bulk spectrum (red trace) decreases dramatically from the spectrum obtained in the reduced region (green trace), indicating a loss of Li in these areas. However, it is also noticed that the low-loss spectra from the TM-reduced area varies among some regions, as shown in Figure S11. The peak located at  $\approx 61.5$ – $62$  eV, which is close to both Li K-edge and Co  $\text{M}_{2,3}$ -edge, is more intense in some regions than the one shown in Figure 4d (green trace). The variation in

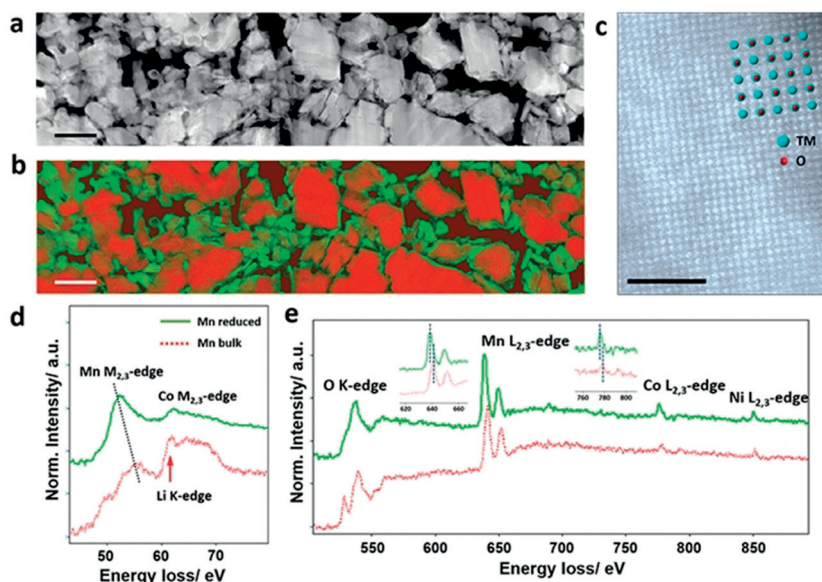


**Figure 4.** Chemical and structural evolution of the 450-cycle LMR-NMC cathode. a) STEM image of the 450-cycle LMR-NMC. b) Valence map of Mn obtained from the region shown in (a); green: Mn reduced to  $2+/3+$ , red: Mn at  $4+$ . The valence map is generated from EELS data using multiple linear least square (MLLS) method; scale bar: 200 nm. c) Atomic-resolution STEM image acquired from the reduced region; scale bar: 2 nm. EELS d) low-loss and e) core-loss spectra acquired from the reduced region (green) and bulk region where Mn maintains  $4+$  (red); the inset in (e) shows the enlarged portion of Mn  $\text{L}_{2,3}$ -edge.

the Li K-edge intensity indicates that there are Li<sup>+</sup> ions existing in some of the reduced regions, which may come from the electrolyte decomposition products, and/or Li-containing distorted phases, that is, defect spinel phase. Nevertheless, most reduced regions suffer severe Li loss and structural transformation that is accompanied by the cation reduction.

The effect of the TM reduction on the performance of the LMR-NMC material was further investigated. First, the redox activities of the Mn, Co and Ni in the first cycle are discussed in detail in the Supporting Information, Figures S12 and S13. Both Co<sup>3+</sup>/Co<sup>4+</sup> and Ni<sup>2+</sup>/Ni<sup>4+</sup> were the major redox couples in the first cycle. Mn<sup>4+</sup> showed no oxidation during the initial charge, and slight reduction during the initial discharge process. This result corroborates other reports.<sup>[14a]</sup> Figure S14 presents the in situ XAS of Co and Ni during the 451<sup>st</sup> cycle. The analysis reveals critical information that Ni is the one that completely loses its electrochemical activity after prolonged cycles, whereas both Mn and Co still display minor redox activities. Yet, it must be noted that the actual capacity delivered by the heavily cycled cell during the in situ measurement was 121 mAhg<sup>-1</sup>; none of the TMs can provide such high capacity according to their XANES measurement. Considering that the in situ XAS was conducted in fluorescence mode, the probing depth should be high enough to reach to the bulk of the material. This discrepancy in the lack of redox activity and high capacity leads to the speculation that oxygen participation is the major source of capacity in this heavily cycled electrode. Previous work has stated that oxygen has a contribution of capacity after 83 cycles; it is possible that this process survives even after 450 cycles.<sup>[15b]</sup> This is a topic beyond the scope of this work. Techniques specializing in probing the state of oxygen, such as resonant inelastic X-ray spectroscopy, will be utilized to further pursue it.

With the above discussions, four major findings can be concluded as summarized in Figure S15. First, FDMNES modeling reveals that a LiMn<sub>2</sub>O<sub>4</sub>-like domain develops during charging, and dissolves during discharging; the size of this domain falls in the range of sub-nanometer. This process is, however, not fully reversible; a certain amount of it survives after each cycle and actual spinel phases can be accumulated after extensive cycles. Therefore, instead of preventing the phase formation by incorporating alien ions as has been done in previous research, it is potentially a good way to explore how to enable full reversibility of the development of LiMn<sub>2</sub>O<sub>4</sub>-like phase. Second, the irreversible TM reduction happens extensively in small-sized particles and on the surface of the large particles. This heterogeneity calls for proper morphology engineering for a better size and structure uniformity. Third, the redox potentials of Co<sup>3+</sup>/Co<sup>4+</sup> and Ni<sup>2+</sup>/Ni<sup>4+</sup> can reach up to 4.5 V. These redox couples become inactive after long-term cycling due to the irreversible reduction of TMs. Without the contribution from these redox couples, the average voltage of the whole process inevitably drops. In order to prevent the valence drop, most of the present studies aimed at either protecting the material surface from direct contact to the electrolyte or stabilizing the O<sup>2-</sup> from loss should be continuously pursued. Fourth, the discrepancy between the actual capacity delivered during the

451<sup>st</sup> cycle and the weak redox activity of the TMs raises a speculation of surviving oxygen activity that needs to be further explored. The method developed in this study by combining FDMNES codes with in situ XANES and TEM-EELS mapping will be highly valuable in the future quest for high-performance electrode materials.

## Acknowledgements

N.C. contributed to the modeling in this work. This research was supported by the Natural Science and Engineering Research Council of Canada (NSERC), the Canada Research Chair Program (CRC), General Motors R&D Center (GM), the Canada Foundation for Innovation (CFI), Canadian Light Source (CLS) at the University of Saskatchewan, the Canadian Centre for Electron Microscopy (CCEM) at McMaster University (a facility supported by the Canada Foundation for Innovation under the Major Science Initiative, NSERC and McMaster University), Beijing Natural Science Foundation (JQ19003), and the University of Western Ontario (UWO).

## Conflict of interest

The authors declare no conflict of interest.

**Keywords:** batteries · Li-ion batteries · spinel domains · TEM/EELS · X-ray absorption spectroscopy

- [1] J. R. Croy, M. Balasubramanian, K. G. Gallagher, A. K. Burrell, *Acc. Chem. Res.* **2015**, *48*, 2813–2821.
- [2] K. A. Jarvis, Z. Deng, L. F. Allard, A. Manthiram, P. J. Ferreira, *Chem. Mater.* **2011**, *23*, 3614–3621.
- [3] a) A. K. Shukla, Q. M. Ramasse, C. Ophus, H. Duncan, F. Hage, G. Chen, *Nat. Commun.* **2015**, *6*, 8711; b) N. Yabuuchi, K. Yoshii, S. T. Myung, I. Nakai, S. Komaba, *J. Am. Chem. Soc.* **2011**, *133*, 4404–4419; c) H. Yu, R. Ishikawa, Y. G. So, N. Shibata, T. Kudo, H. Zhou, Y. Ikuhara, *Angew. Chem. Int. Ed.* **2013**, *52*, 5969–5973; *Angew. Chem.* **2013**, *125*, 6085–6089; d) K. Zhang, B. Li, Y. Zuo, J. Song, H. Shang, F. Ning, D. Xia, *Electrochem. Energy Rev.* **2019**, *2*, 606–623; e) Y. Ding, Z. P. Cano, A. Yu, J. Lu, Z. Chen, *Electrochem. Energy Rev.* **2019**, *2*, 1–28.
- [4] L. Gu, D. Xiao, Y. S. Hu, H. Li, Y. Ikuhara, *Adv. Mater.* **2015**, *27*, 2134–2149.
- [5] a) M. Sathiyaa, A. M. Abakumov, D. Foix, G. Rousse, K. Ramesha, M. Saubanere, M. L. Doublet, H. Vezin, C. P. Laisa, A. S. Prakash, D. Gonbeau, G. VanTendeloo, J. M. Tarascon, *Nat. Mater.* **2015**, *14*, 230–238; b) B. Xiao, X. Sun, *Adv. Energy Mater.* **2018**, *8*, 1802057–1802083.
- [6] a) H. Yu, H. Zhou, *J. Phys. Chem. Lett.* **2013**, *4*, 1268–1280; b) P. Yan, J. Zheng, J. Zheng, Z. Wang, G. Teng, S. Kuppan, J. Xiao, G. Chen, F. Pan, J.-G. Zhang, C.-M. Wang, *Adv. Energy Mater.* **2016**, *6*, 1502455–1502463; c) P. Yan, A. Nie, J. Zheng, Y. Zhou, D. Lu, X. Zhang, R. Xu, I. Belharouak, X. Zu, J. Xiao, K. Amine, J. Liu, F. Gao, R. Shahbazian-Yassar, J. G. Zhang, C. M. Wang, *Nano Lett.* **2015**, *15*, 514–522; d) M. Gu, I. Belharouak, J. Zheng, H. Wu, J. Xiao, A. Genc, K. Amine, S. Thevuthasan, D. R. Baer, J. G. Zhang, N. D. Browning, J. Liu, C. Wang, *ACS Nano* **2013**, *7*, 760–767.

- [7] a) J. Zheng, P. Xu, M. Gu, J. Xiao, N. D. Browning, P. Yan, C. Wang, J.-G. Zhang, *Chem. Mater.* **2015**, *27*, 1381–1390; b) J. Zheng, M. Gu, A. Genc, J. Xiao, P. Xu, X. Chen, Z. Zhu, W. Zhao, L. Pullan, C. Wang, J. G. Zhang, *Nano Lett.* **2014**, *14*, 2628–2635; c) X. Yu, Y. Lyu, L. Gu, H. Wu, S.-M. Bak, Y. Zhou, K. Amine, S. N. Ehrlich, H. Li, K.-W. Nam, X.-Q. Yang, *Adv. Energy Mater.* **2014**, *4*, 1300950–1300960; d) H. Yu, Y. G. So, A. Kuwabara, E. Tochigi, N. Shibata, T. Kudo, H. Zhou, Y. Ikuhara, *Nano Lett.* **2016**, *16*, 2907–2915.
- [8] a) H. Yu, Y. G. So, Y. Ren, T. Wu, G. Guo, R. Xiao, J. Lu, H. Li, Y. Yang, H. Zhou, R. Wang, K. Amine, Y. Ikuhara, *J. Am. Chem. Soc.* **2018**, *140*, 15279–15289; b) S. Hy, H. Liu, M. Zhang, D. Qian, B.-J. Hwang, Y. S. Meng, *Energy Environ. Sci.* **2016**, *9*, 1931–1954.
- [9] R. Malik, *Joule* **2017**, *1*, 647–648.
- [10] A. R. Armstrong, N. Dupre, A. J. Paterson, C. P. Grey, P. G. Bruce, *Chem. Mater.* **2004**, *16*, 3106–3118.
- [11] P. Lu, P. Yan, E. Romero, E. D. Spoecker, J.-G. Zhang, C.-M. Wang, *Chem. Mater.* **2015**, *27*, 1375–1380.
- [12] a) T. Waldmann, A. Iturrondobetia, M. Kasper, N. Ghanbari, F. Aguesse, E. Bekaert, L. Daniel, S. Genies, I. J. Gordon, M. W. Löble, E. De Vito, M. Wohlfahrt-Mehrens, *J. Electrochem. Soc.* **2016**, *163*, A2149–A2164; b) J. Cabana, S.-H. Kang, C. S. Johnson, M. M. Thackeray, C. P. Grey, *J. Electrochem. Soc.* **2009**, *156*, A730.
- [13] a) B. Ammundsen, D. J. Jones, J. Rozière, G. R. Burns, *Chem. Mater.* **1996**, *8*, 2799–2808; b) Y. Arachi, H. Kobayashi, S. Emura, Y. Nakata, M. Tanaka, T. Asai, *Phys. Scr.* **2005**, 577–579; c) M. Balasubramanian, X. Sun, X. Q. Yang, J. McBreen, *J. Electrochem. Soc.* **2000**, *147*, 2903–2909; d) B. Xiao, J. Liu, Q. Sun, B. Wang, M. N. Banis, D. Zhao, Z. Wang, R. Li, X. Cui, T. K. Sham, X. Sun, *Adv. Sci.* **2015**, *2*, 1500022–1500027; e) B. Xiao, H. Liu, J. Liu, Q. Sun, B. Wang, K. Kaliyappan, Y. Zhao, M. N. Banis, Y. Liu, R. Li, T. K. Sham, G. A. Botton, M. Cai, X. Sun, *Adv. Mater.* **2017**, *29*, 1703764–1703775.
- [14] a) A. Ito, Y. Sato, T. Sanada, M. Hatano, H. Horie, Y. Ohsawa, *J. Power Sources* **2011**, *196*, 6828–6834; b) K. Luo, M. R. Roberts, R. Hao, N. Guerrini, D. M. Pickup, Y. S. Liu, K. Edstrom, J. Guo, A. V. Chadwick, L. C. Duda, P. G. Bruce, *Nat. Chem.* **2016**, *8*, 684–691; c) H. Koga, L. Croguennec, M. Ménétrier, P. Mannezzies, F. Weill, C. Delmas, S. Belin, *J. Phys. Chem. C* **2014**, *118*, 5700–5709; d) T. Kim, B. H. Song, A. J. G. Lunt, G. Cibin, A. J. Dent, L. Lu, A. M. Korsunsky, *Chem. Mater.* **2016**, *28*, 4191–4203.
- [15] a) D. H. Seo, J. Lee, A. Urban, R. Malik, S. Kang, G. Ceder, *Nat. Chem.* **2016**, *8*, 692–697; b) E. Hu, X. Yu, R. Lin, X. Bi, J. Lu, S. Bak, K.-W. Nam, H. L. Xin, C. Jaye, D. A. Fischer, K. Amine, X.-Q. Yang, *Nat. Energy* **2018**, *3*, 690–698; c) Y. N. Zhou, J. L. Yue, E. Hu, H. Li, L. Gu, K. W. Nam, S. M. Bak, X. Yu, J. Liu, J. Bai, E. Dooryhee, Z. W. Fu, X. Q. Yang, *Adv. Energy Mater.* **2016**, *6*, 1600597–1600604; d) L. Simonin, J.-F. Colin, V. Ranier, E. Canévet, J.-F. Martin, C. Bourbon, C. Baetz, P. Strobel, L. Daniel, S. Patoux, *J. Mater. Chem.* **2012**, *22*, 11316–11322.
- [16] a) M. Newville, *J. Synchrotron Radiat.* **2001**, *8*, 322–324; b) Y. Joly, O. Bunău, J. E. Lorenzo, R. M. Galéra, S. Grenier, B. Thompson, *J. Phys. Conf. Ser.* **2009**, *190*, 012007–012019.
- [17] S. Hy, F. Felix, J. Rick, W. N. Su, B. J. Hwang, *J. Am. Chem. Soc.* **2014**, *136*, 999–1007.
- [18] a) S. Hy, J.-H. Cheng, J.-Y. Liu, C.-J. Pan, J. Rick, J.-F. Lee, J.-M. Chen, B. J. Hwang, *Chem. Mater.* **2014**, *26*, 6919–6927; b) D. Mohanty, J. Li, S. C. Nagpure, D. L. Wood, C. Daniel, *MRS Energy Sustainability* **2015**, *2*, 1–24; c) H. Liu, K. J. Harris, M. Jiang, Y. Wu, G. R. Goward, G. A. Botton, *ACS Nano* **2018**, *12*, 2708–2718.
- [19] R. Shunmugasundaram, R. Senthil Arumugam, J. R. Dahn, *Chem. Mater.* **2015**, *27*, 757–767.
- [20] Y. Bi, T. Wang, M. Liu, R. Du, W. Yang, Z. Liu, Z. Peng, Y. Liu, D. Wang, X. Sun, *RSC Adv.* **2016**, *6*, 19233–19237.
- [21] a) W. S. Yoon, M. Balasubramanian, K. Y. Chung, X. Q. Yang, J. McBreen, C. P. Grey, D. A. Fischer, *J. Am. Chem. Soc.* **2005**, *127*, 17479–17487; b) C. Rumble, T. E. Conry, M. Doeff, E. J. Cairns, J. E. Penner-Hahn, A. Deb, *J. Electrochem. Soc.* **2010**, *157*, A1317–A1322; c) M. Oishi, T. Fujimoto, Y. Takamashi, Y. Orikasa, A. Kawamura, T. Ina, H. Yamashige, D. Takamatsu, K. Sato, H. Murayama, H. Tanida, H. Arai, H. Ishii, C. Yogi, I. Watanabe, T. Ohta, A. Mineshige, Y. Uchimoto, Z. Ogumi, *J. Power Sources* **2013**, *222*, 45–51; d) K. Luo, M. R. Roberts, N. Guerrini, N. Tapia-Ruiz, R. Hao, F. Massel, D. M. Pickup, S. Ramos, Y. S. Liu, J. Guo, A. V. Chadwick, L. C. Duda, P. G. Bruce, *J. Am. Chem. Soc.* **2016**, *138*, 11211–11218.
- [22] Y. Joly, *Phys. Rev. B* **2001**, *63*, 125120–125119.
- [23] T. E. Conry, A. Mehta, J. Cabana, M. M. Doeff, *J. Electrochem. Soc.* **2012**, *159*, A1562–A1571.
- [24] D. Mohanty, J. Li, D. P. Abraham, A. Huq, E. A. Payzant, D. L. Wood, C. Daniel, *Chem. Mater.* **2014**, *26*, 6272–6280.
- [25] C. P. Grey, W.-S. Yoon, J. Reed, G. Ceder, *Electrochem. Solid-State* **2004**, *7*, A290–A293.
- [26] K. G. Gallagher, J. R. Croy, M. Balasubramanian, M. Bettge, D. P. Abraham, A. K. Burrell, M. M. Thackeray, *Electrochem. Commun.* **2013**, *33*, 96–98.
- [27] B. Xiao, B. Wang, J. Liu, K. Kaliyappan, Q. Sun, Y. Liu, G. Dadheech, M. P. Balogh, L. Yang, T.-K. Sham, R. Li, M. Cai, X. Sun, *Nano Energy* **2017**, *34*, 120–130.
- [28] a) H. Chen, M. S. Islam, *Chem. Mater.* **2016**, *28*, 6656–6663; b) D. Ye, G. Zeng, K. Nogita, K. Ozawa, M. Hankel, D. J. Searles, L. Wang, *Adv. Funct. Mater.* **2015**, *25*, 7488–7496; c) L. de Biasi, B. Schwarz, T. Brezesinski, P. Hartmann, J. Janek, H. Ehrenberg, *Adv. Mater.* **2019**, *31*, 1900985–1901018.
- [29] a) W. Hua, M. Chen, B. Schwarz, M. Knapp, M. Bruns, J. Barthel, X. Yang, F. Sigel, R. Azmi, A. Senyshyn, A. Missiul, L. Simonelli, M. Etter, S. Wang, X. Mu, A. Fiedler, J. R. Binder, X. Guo, S. Chou, B. Zhong, S. Indris, H. Ehrenberg, *Adv. Energy Mater.* **2019**, *9*, 1803094–1803103; b) N. Li, S. Hwang, M. Sun, Y. Fu, V. S. Battaglia, D. Su, W. Tong, *Adv. Energy Mater.* **2019**, *9*, 1902258–1902265; c) J. Zhang, F. Cheng, S. Chou, J. Wang, L. Gu, H. Wang, H. Yoshikawa, Y. Lu, J. Chen, *Adv. Mater.* **2019**, *31*, 1901808–1901814.
- [30] P. Yan, J. Zheng, Z. K. Tang, A. Devaraj, G. Chen, K. Amine, J. G. Zhang, L. M. Liu, C. Wang, *Nat. Nanotechnol.* **2019**, *14*, 602–608.
- [31] A. S. Aricò, P. Bruce, B. Scrosati, J. M. Tarascon, W. van Schalkwijk, *Nat. Mater.* **2005**, *4*, 366–377.
- [32] A. Boulineau, L. Simonin, J.-F. Colin, C. Bourbon, S. Patoux, *Nano Lett.* **2013**, *13*, 3857–3863.

Manuscript received: April 12, 2020

Revised manuscript received: May 27, 2020

Accepted manuscript online: May 28, 2020

Version of record online: June 30, 2020